Toughening Elastomers with Sacrificial Bonds and Watching Them Break

Etienne Ducrot,[1,2,3] Yulan Chen,[4] Markus Bulters,[5] Rint P. Sijbesma,[4] Costantino Creton[1,2,3]*

Elastomers are widely used because of their large-strain reversible deformability. Most unfilled elastomers suffer from a poor mechanical strength, which limits their use. Using sacrificial bonds, we show how brittle, unfilled elastomers can be strongly reinforced in stiffness and toughness (up to 4 megapascals and 9 kilojoules per square meter) by introducing a variable proportion of isotropically prestretched chains that can break and dissipate energy before the material fails. Chemoluminescent cross-linking molecules, which emit light as they break, map in real time where and when many of these internal bonds break ahead of a propagating crack. The simple methodology that we use to introduce sacrificial bonds, combined with the mapping of where bonds break, has the potential to stimulate the development of new classes of unfilled tough elastomers and better molecular models of the fracture of soft materials.

Elastomers are widely used in industrial applications such as tires, seals, gloves, and dampers for their ability to deform reversibly to large strains. Yet currently, maintaining this large deformability imposes an upper limit in stiffness. Above a Young's modulus of around 1 to 1.5 MPa, unfilled elastomers are brittle, limiting applications. This limitation is particularly severe at high temperatures and for rubbers with a low entanglement density. Fracture of simple elastomers has been described by Lake and Thomas (*1*, *2*), who predicted that the threshold fracture toughness (minimum energy necessary to break the elastomer) should scale with $N_c^{1/2}$, where N_c is the number of monomers between cross-links. In essence, the more cross-linked (and the stiffer) the elastomer, the more brittle it becomes. To circumvent this limitation, rubbers have been toughened by adding nanofillers and by making the elastomers more viscoelastic (*3*). It was found that optimized nanofillers impart a large increase in stiffness at small strain and cause highly dissipative processes to be active at large strains, effectively increasing both stiffness and strain at break (*4*). However, incorporating nanofillers introduces constraints in terms of processing and safety and requires careful dispersion. Alternatively, increasing the viscoelastic character of the elastomer is used to increase fracture toughness through molecular friction (*5*), but this method only works over a limited temperature range.

Many empirical strategies have been tried to increase simultaneously the strength and stiffness of unfilled elastomers by introducing heterogeneities in the network. The multimodal distribution of molecular weights between cross-links has been extensively tried on silicones, but the gains in stiffness at low strains only result in moderate increases in toughness (*6*–*8*). Another strategy has been to prestretch a partially cross-linked elastomer and further cross-link it in the stretched state (*9*). This improves the strength of the elastomer in the prestretching direction but decreases the initial tensile modulus and leads to very anisotropic properties. Knowledge-based strategies to increase fracture toughness while retaining full reversibility of deformation and low viscoelasticity have been limited by the lack of understanding of where and how energy is dissipated as a crack propagates. This micromechanical knowledge has been developed decades ago for materials with a yield stress, such as metals (*10*) and glassy polymers (*11*, *12*), in which dissipation of energy is localized and visible in a plastically deformed zone. However, for soft materials (gels, rubbers, or soft adhesives) there is typically no well-defined yield stress, and the origin of dissipation of energy during crack propagation remains an open question. Recent work has shown hydrogels with toughness in excess of 100 to 1000 times that of regular (very brittle) gels while maintaining a reasonable extensibility and recoverability of the strain (*13*, *14*). Hydrogels are very soft [Young's modulus (E) 1 to 100 kPa] molecular sponges full of water and thus are quite different materials from the hydrophobic and fully water-insoluble elastomers. The increase in toughness has been attributed there to the early fracture of "weak or overstressed" bonds (either intrinsically weaker than the main bonds, or loaded more than the main bonds) introduced in the bulk of the material by means of the synthetic method (*13*, *15*–*17*).

Our elastomers are obtained through sequential free-radical polymerizations. First, a well–cross-linked rubbery network is synthesized by means of ultraviolet (UV) polymerization in the presence of solvent. After drying, the rubber sheet referred to as "single network" (SN) is then swollen with a second monomer, UV initiator, and a small amount of cross-linker, effectively isotropically stretching the chains of the network. A second UV polymerization is performed on this swollen network, until all monomer is consumed. Varying the degree of cross-linking of the first network controls the level of swelling from a swelling ratio (Q) = 3.3 to 5 and effectively controls the level of prestretch of the first network chains and their volume fraction in the network (fig. S1). The double networks will be referred to as "DN." To obtain even lower-volume fractions of first network and higher levels of prestretch, the second step can be repeated on the DN. The presence of chains of the second network decrease the elastic component of the free energy per unit volume, allowing us to stretch first network chains further. The third polymerization step results in a material in which the first network chains only represent 5 to 10 weight percent (wt %) and are highly stretched, whereas the chains polymerized during the second step are lightly stretched, and those polymerized during the third step are entangled, lightly cross-linked, and loosely connected by chain transfer reactions (fig. S2 and table S3). These triple networks will be referred to as TN. It should be noted that because of the nature of the monomers used (acrylates), chain transfer reactions to the polymer likely occur during the second and third polymerization, effectively loosely connecting the networks with each other and affecting stress transfer between the networks.

In our example, the first network is made from ethyl acrylate and butanediol diacrylate cross-linker, and the second and third steps have

Table 1. Composition and properties of the materials of the study. Shown are the temperature of the experiment T, weight fraction of first network $\phi_{wt\%}^{1st}$, Young's modulus E (in MPa), and true stress at break σ_T^{break} (in MPa). Dashes indicate that the measurement was not done for that network.

Sample	T (°C)	SN EA_x			DN EA_xMA			TN EA_xMAMA		
First network		$\phi_{wt\%}^{1st}$	E	σ_T^{break}	$\phi_{wt\%}^{1st}$	E	σ_T^{break}	$\phi_{wt\%}^{1st}$	E	σ_T^{break}
$EA_{0.5}$	60	100	0.8	0.5	20	1.3	8	6	2.2	22
EA_1	60	100	1.5	0.5	30	2	6.5	10	4.2	29
EA_2	60	100	2.3	0.5	35	2.3	3	—	—	—
		SN $EA_{0.5}$			DN $EA_{0.5}EA$			TN $EA_{0.5}EAEA$		
$EA_{0.5}$	20	100	0.6	1.2	20	0.8	10	5	1.5	16

[1]École Supérieure de Physique et de Chimie Industrielles de la Ville de Paris (ESPCI) ParisTech, UMR 7615, 10, Rue Vauquelin, 75231 Paris Cédex 05, France. [2]CNRS, UMR 7615, 10, Rue Vauquelin, 75231 Paris Cédex 05, France. [3]Sorbonne-Universités, Université Pierre et Marie Curie (UPMC) Université Paris 06, UMR 7615, 10, Rue Vauquelin, 75231 Paris Cédex 05, France. [4]Institute for Complex Molecular Systems, Eindhoven University of Technology, Post Office Box 513, 5600 MB Eindhoven, Netherlands. [5]DSM Ahead, Urmonderbaan 22, 6167 RD Geleen, Netherlands.

*Corresponding author. E-mail: costantino.creton@espci.fr

been carried out with methyl acrylate. However, similar networks have been obtained with sequential polymerizations by using two methyl acrylate networks or two and three ethyl acrylate networks with similar results (fig. S3 and table S1). A summary of the properties and nomenclature of the materials is shown in Table 1. Three cross-linker concentrations in the first network are presented here (table S1). $EA_{0.5}$ is cross-linked at 1.45 mole percent (mol %) of monomer, EA_1 two times more (2.81 mol %), and EA_2 four times more (5.81 mol %). Their corresponding DN and TN are referred to as EA_xMA if the second network is made of MA or EA_xEA if the second monomer is EA, and referred to as EA_xMAMA if the third network is made of MA or EA_xEAEA if the third monomer is EA.

As an example of the mechanical properties of SN, DN, and TN elastomers, the stress strain curves at 60°C [45°C above the glass transition temperature (T_g) of the PMA] in uniaxial extension are shown in Fig. 1A for EA_1, EA_1MA, and EA_1MAMA. The elastic modulus of the elastomer increases by a factor of up to 3.5, whereas the true stress at break increases by a factor of 58. The effect of changing the cross-linker concentration in the first network on the properties of the DN elastomer is shown in Fig. 1B, and the effect of changing the second and third monomer for the DN and TN materials [at equal temperature difference from Tg. ($T - T_g$)] is shown in Fig. 1C. In principle, such a striking increase in strength could be due to plasticity in large strain, leading to permanent deformation upon unloading.

However, as shown in Fig. 2A the material unloads with no detectable hysteresis for the EA_1MA DN, and as shown in Fig. 2B, there is a substantial hysteresis during the first cycle but no measurable hysteresis for the subsequent cycles to the same strain for the $EA_{0.5}MAMA$ TN. The residual deformation after each cycle remains below 6% for the DN and TN, and the modulus after each cycle remains nearly constant for the TN, showing that the damage is very moderate (fig. S4). Although substantial hysteresis occurs in the material in cyclic extension, the modulus does not decrease much. This suggests that unlike what was observed for gels, most of the initial modulus is due to the second and third network, and the chains of the first network simply limit the maximum extensibility.

The increase in strain and stress at break suggests that the fracture toughness of the elastomers should also increase. We carried out crack propagation experiments on single-edged notched samples (fig. S5) at a low nominal strain rate of 0.025 s^{-1} at 60°C and 20°C for all prepared networks and used the large-strain approximation of Greensmith (*18*) to extract the critical energy release rate G_c. The results are presented in Fig. 3 as a function of the elastic modulus. The fracture toughness G_c increases from ~50 J/m^2 to 2000 to 5000 J/m^2 from the SN and the TN. These values of fracture toughness for materials that also have a high elastic modulus and low loading rate is in the range of some filled elastomers or of the best tough hydrogels. We are aware of one unfilled elastomer that has a comparable combination of properties—namely, natural rubber, which reaches a G_c value of 2 to 10 kJ/m^2 in comparable conditions (*19*). But, this behavior is due to strain-induced crystallization, which is difficult to reproduce in other elastomers.

We hypothesize that the origin of the toughening mechanism is similar to that of Gong and coworkers (*15*, *20*, *21*)—that the fracture of covalent bonds in the primary-minority network controls the stress level (and hence the stiffness), whereas the second- and third-majority networks prevent large cracks from forming. From macroscopic evidence, Gong and coworkers could assess that bonds actually break near the crack tip.

We found that we can directly see where and when sacrificial bonds break as the material is deformed by using a chemoluminescent

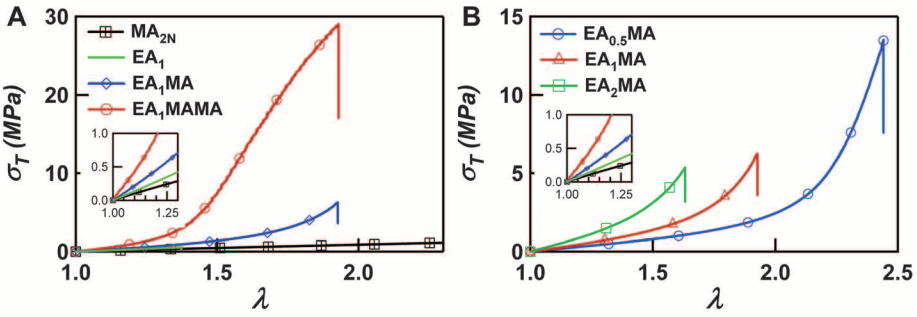

Fig. 1. Mechanical behavior of tough elastomers in uniaxial tension. (**A**) True stress/stretch curves of the EA_1, EA_1MA, EA_1MAMA, and PMA second network alone at 60°C. (**B**) Effect of changing the level of cross-linker in the EA first network on the EA_xMA DN. (**C**) Comparisons between $EA_{0.5}MA$[MA] and $EA_{0.5}EA$[EA] at equivalent $T - T_g$. Solid lines represent the TN, and dashed lines represent the DN.

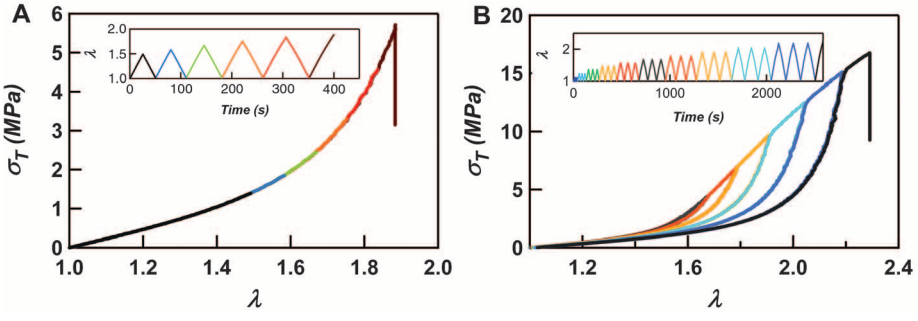

Fig. 2. Step-cycle loading-unloading curves of multiple network elastomers at 60°C. (**A**) Stress-strain curve of a single sample of EAMA elastomer submitted to a step-cycle loading. (Inset) The applied stretch as a function of time. All curves follow the same path on the σ-λ curve for this elastomer. (**B**) The same graph for a single sample of $EA_{0.5}MAMA$ network. In this case, each *n*th cycle follows a different path when λ of the *n*th cycle exceeds the maximum value of λ of the $(n - 1)$ cycle. Despite the damage in large strain, the initial modulus is nearly the same for all cycles (fig. S4).

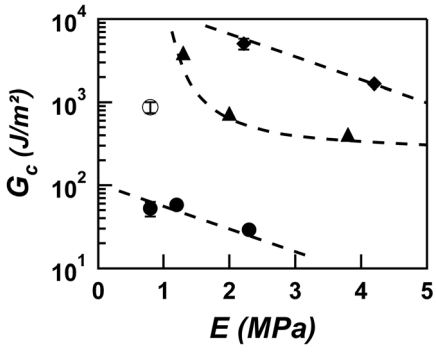

Fig. 3. Fracture toughness of multiple network elastomers. Shown is the fracture toughness G_c from single-edge notch tests at 60°C versus initial modulus for SN (solid circles), DN (triangles), and TN (diamonds) of various cross-linker concentrations in the first network EA_x[MA[MA]], second network alone MA_{2N} (open circle). The dashed lines are to guide the eyes. Error bars show SD; sample size, $n = 3$ repeats per experiment.

cross-linker, bis(adamantyl)-1,2-dioxetane bisacrylate (BADOBA) (fig. S6) (*22*), which is able to emit light when it breaks. If a sufficient force is applied to the BADOBA, the dioxetane group breaks into two ketones, one of which is in the excited state, as shown schematically in Fig. 4A. Relaxation to the ground state emits a photon in the bright blue range of the spectrum (emission maximum Λ_{max} = 420 nm). Because MA-based networks need to be tested at 60°C and the BADOBA is insufficiently stable at 60°C for the duration of a mechanical test, we chose fully EA-based networks and prepared a SN of $EA_{0.5}$, a DN of $EA_{0.5}EA$, and a TN of $EA_{0.5}EAEA$. In all of these networks, the first network was cross-linked with BADOBA. Uniaxial tensile cycles and fracture tests were filmed with a sensitive camera able to detect single photons at 50 images per second (fig. S7). The load-unload cycles of an $EA_{0.5}EA$ DN is shown in Fig. 4B, together with the corresponding light emission signal as a function of λ, and the same data for the TN network is shown in Fig. 4, C and D. A video of the luminescence of TN under cyclic extension is presented in movie S1. Bond breakage only occurs above a certain value of λ, and only for the first cycle, because subsequent cycles to the same value of λ are fully elastic. This data demonstrate that the first-cycle hysteresis (fig. S8) is due to the irreversible breakage of bonds homogeneously in the whole sample. Comparing the mechanical data of Fig. 4, B and C, with that of Fig. 1C, the replacement of the BDA with the BADOBA only has a small weakening effect on the mechanical properties of the elastomers, strongly suggesting that although the chemoluminescent bond is a bit weaker than a C-C bond (150 kJ/mol versus 350 kJ/mol) (*23*), it really acts as a marker and does not modify the mechanism itself. The power-law correlation between the cumulative mechanical hysteresis and the total emitted light for a given value of λ is shown in Fig. 4E.

Having established that the intensity of blue light is directly connected to the mechanical hysteresis, the next step was to use it to map bond breakage during fracture experiments. The image of the luminescence around the tip of a propagating crack is shown in Fig. 5 for the EA-based SN, DN, and TN. A video of the crack propagation in the TN followed by chemoluminescence is presented in movie S2. Because scales are identical and the signal is proportional to the number of photons per pixel, the intensity can be compared; the bond breakage is very localized in front of the crack tip (practically one pixel) for the SN, is still localized at the crack tip but more intense for the DN, and extends over a large region in the material for the TN. A precise integration of the luminescence over the whole region is not possible because of the high dynamic range, leading to a saturation of the camera sensor. However, these results show that the same mechanism detected by the hysteresis in uniaxial tension is active at the crack tip. This result is in qualitative agreement with post mortem observations on fractured gels (*20*) and with two models proposed respectively by Tanaka (*24*) and Brown (*25*), predicting that the dual population of co-continuous networks creates a yielding mechanism and a damage zone where the yield stress is controlled by the stress to break the first network bonds, and the size of the zone is controlled by the extensibility of the second network chains.

However, the intensity mapping provides much more precise information. It shows that an increase in degree of prestretching of the chains and a decrease in their volume fraction leads to a much

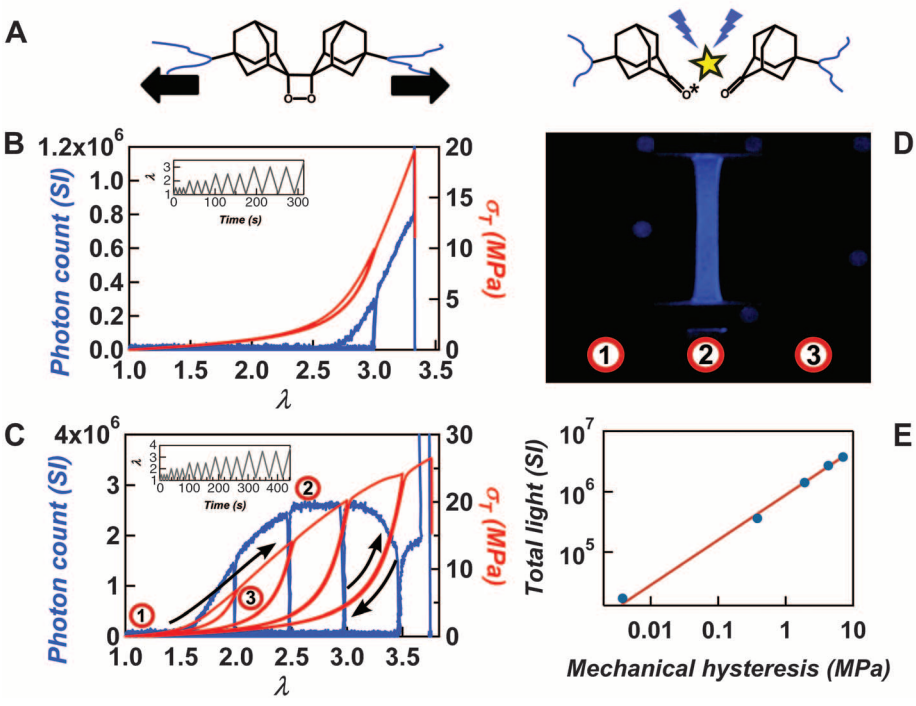

Fig. 4. Chemoluminescent molecules to detect bond breakage. (**A**) Schematic of the chemoluminescence process, bond breakage of the dioxetane cross-linker, and light emission. (**B**) Step-cycle test for a single sample of the DN network showing mechanical stress-strain curves (red) and light emission curves measured with image analysis (blue) for the same sample. A slight amount of bond breakage is observed at high strain. (**C**) Step-cycle test for a single sample of the TN network showing light emission (in blue) and stress (in red). Light emission is zero during unloading and reloading, until λ of the *n*th cycle exceeds the maximum value of λ of the (*n* − 1) cycle. (**D**) Image of the luminescence of TN under loading at various steps of the experiment [reported in (C)]: (1) near the beginning of the test, (2) on the first loading at λ ~ 2.6, and (3) on reloading at λ ~ 1.7. (**E**) Cumulative light emitted during the cycles as a function of the mechanical hysteresis in TN. The mechanical hysteresis is defined as sum of the integrals under load-unload cycles, and the total light is the sum of the emitted light for that level of mechanical hysteresis. The total light varies as the mechanical hysteresis to the power 0.75.

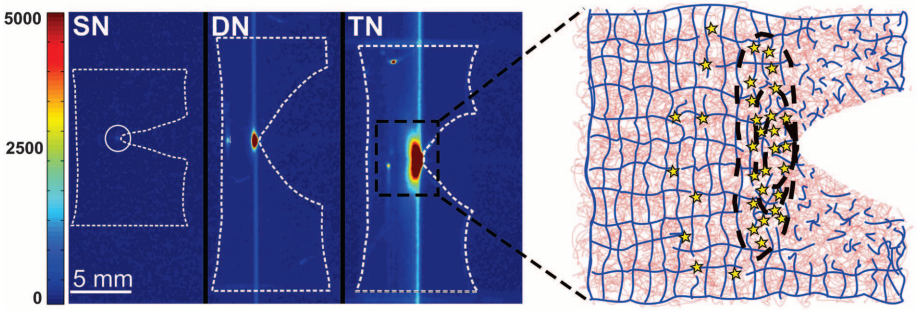

Fig. 5. Mapping of where bonds break during crack propagation. Intensity-colorized images of propagating cracks on notched samples containing dioxetane cross-linker in the first network, showing the light emission due to the breakage of bonds in SN, DN, and TN samples. The size and geometry of the sample are shown with a white dashed line. Vertical lines in the DN and TN image are due to detector artifacts; in DN and TN, spots far from the crack tip are due to reflection of the light on surface inhomogeneities and do not correspond to a local light emission. (Right) Schematic of the sacrificial bond-breaking mechanism in front of the crack tip for the DN and TN; the first network is represented in blue, and the second and third networks are in red.

larger dissipative volume ahead of the crack tip and to a tougher material, therefore guiding materials design. It also shows the dynamic shape of the damage zone, allowing a quantitative comparison with more advanced damage models (*26*).

A family of tough, stiff unfilled elastomers with less than 6% of residual deformation after strains up to 150%, and negligible viscoelasticity, can be obtained from ordinarily brittle elastomers. The toughening mechanism relies on the dissipation of energy due to bond breakage of a variable fraction of sacrificial prestretched chains inside the material. By varying the volume fraction, monomer type, and cross-linking level of the prestretched chains, the properties of the materials can be tuned over a wide range, and design can be guided by the concomitant use of chemoluminescent molecules to reveal where and when bonds break during fracture. The methodology can be used both to develop better models of fracture of soft materials and to guide design of other families of soft materials than polyacrylics, which have ordinarily poor mechanical properties but much better resistance to temperature, UV, or chemicals.

References and Notes

1. G. J. Lake, P. B. Lindley, *J. Appl. Polym. Sci.* **9**, 1233–1251 (1965).
2. G. J. Lake, A. G. Thomas, *Proc. R. Soc. Lond. A Math. Phys. Sci.* **300**, 108–119 (1967).
3. A. N. Gent, *Langmuir* **12**, 4492–4496 (1996).
4. G. Heinrich, M. Kluppel, T. A. Vilgis, *Curr. Opin. Solid St. M.* **6**, 195–203 (2002).
5. B. N. J. Persson, O. Albohr, G. Heinrich, H. Ueba, *J. Phys. Condens. Matter* **17**, R1071–R1142 (2005).
6. B. D. Viers, J. E. Mark, *J. Macromol. Sci. Part A Pure Appl. Chem.* **44**, 131–138 (2007).
7. G. D. Genesky, C. Cohen, *Polymer (Guildf.)* **51**, 4152–4159 (2010).
8. G. D. Genesky, B. M. Aguilera-Mercado, D. M. Bhawe, F. A. Escobedo, C. Cohen, *Macromolecules* **41**, 8231–8241 (2008).
9. N. K. Singh, A. J. Lesser, *Macromolecules* **44**, 1480–1490 (2011).
10. G. E. Dieter, *Mechanical Metallurgy* (McGraw Hill, New York, ed. 2, 1976).
11. H. R. Brown, *Macromolecules* **24**, 2752–2756 (1991).
12. E. J. Kramer, L. L. Berger, *Adv. Polym. Sci.* **91**, 1–68 (1990).
13. J. P. Gong, Y. Katsuyama, T. Kurokawa, Y. Osada, *Adv. Mater.* **15**, 1155–1158 (2003).
14. Y. Tanaka *et al.*, *J. Phys. Chem. B* **109**, 11559–11562 (2005).
15. R. E. Webber, C. Creton, H. R. Brown, J. P. Gong, *Macromolecules* **40**, 2919–2927 (2007).
16. J.-Y. Sun *et al.*, *Nature* **489**, 133–136 (2012).
17. Y. H. Na *et al.*, *Macromolecules* **39**, 4641–4645 (2006).
18. H. W. Greensmith, *J. Appl. Polym. Sci.* **7**, 993–1002 (1963).
19. K. Sakulkaew, A. G. Thomas, J. J. C. Busfield, *Polym. Test.* **30**, 163–172 (2011).
20. Q. M. Yu, Y. Tanaka, H. Furukawa, T. Kurokawa, J. P. Gong, *Macromolecules* **42**, 3852–3855 (2009).
21. T. Nakajima, T. Kurokawa, S. Ahmed, W.- Wu, J. P. Gong, *Soft Matter* **9**, 1955–1966 (2013).
22. Y. Chen *et al.*, *Nat. Chem.* **4**, 559–562 (2012).
23. P. Lechtken, *Chem. Ber.* **109**, 2862–2870 (1976).
24. Y. Tanaka, *Europhys. Lett.* **78**, 56005 (2007).
25. H. R. Brown, *Macromolecules* **40**, 3815–3818 (2007).
26. X. Wang, W. Hong, *Soft Matter* **7**, 8576–8581 (2011).

Acknowledgments: We gratefully acknowledge the financial support of DSM Ahead, Geleen, Netherlands and many helpful discussions with the researchers of their Materials Science Center. We also thank E.J. Kramer and H.R. Brown for their insightful comments and critical reading of the manuscript, and D. Martina for his friendly and efficient help in setting up the camera for the chemoluminescence experiments. Last, we thank W. Fresquet from Andor Technology for lending us the camera.

Supplementary Materials

www.sciencemag.org/content/344/6180/186/suppl/DC1
Materials and Methods
Supplementary Text
Figs. S1 to S7
Tables S1 to S3
Reference (*27*)
Movies S1 to S2

13 November 2013; accepted 6 March 2014
10.1126/science.1248494

Mitosis Inhibits DNA Double-Strand Break Repair to Guard Against Telomere Fusions

Alexandre Orthwein,[1] Amélie Fradet-Turcotte,[1] Sylvie M. Noordermeer,[1] Marella D. Canny,[1] Catherine M. Brun,[1] Jonathan Strecker,[1,2] Cristina Escribano-Diaz,[1] Daniel Durocher[1,2]*

Mitotic cells inactivate DNA double-strand break (DSB) repair, but the rationale behind this suppression remains unknown. Here, we unravel how mitosis blocks DSB repair and determine the consequences of repair reactivation. Mitotic kinases phosphorylate the E3 ubiquitin ligase RNF8 and the nonhomologous end joining factor 53BP1 to inhibit their recruitment to DSB-flanking chromatin. Restoration of RNF8 and 53BP1 accumulation at mitotic DSB sites activates DNA repair but is, paradoxically, deleterious. Aberrantly controlled mitotic DSB repair leads to Aurora B kinase–dependent sister telomere fusions that produce dicentric chromosomes and aneuploidy, especially in the presence of exogenous genotoxic stress. We conclude that the capacity of mitotic DSB repair to destabilize the genome explains the necessity for its suppression during mitosis, principally due to the fusogenic potential of mitotic telomeres.

We hypothesized that the inactivation of mitotic double-strand break (DSB) repair (*1*–*3*) might be caused by the failure to recruit the DSB repair factors BRCA1 and 53BP1 to DNA damage sites during mitosis (*4*–*7*). 53BP1 and BRCA1 promote DSB repair by nonhomologous end joining (NHEJ) and homologous recombination, respectively (*8*). Both proteins accumulate at DSB sites downstream of a common pathway consisting of the ataxia telangiectasia mutated–dependent phosphorylation of H2AX (forming γ-H2AX) followed by MDC1, RNF8, and RNF168 recruitment (*8*). RNF168 ubiquitylates H2A (*9*, *10*), which triggers the recruitment of 53BP1 (*11*) and also BRCA1 (*12*). Mitosis severs this pathway upstream of RNF8 recruitment to DSB sites as the formation of γ-H2AX and MDC1 ionizing radiation (IR)–induced foci, which denote accumulation at break sites, are unaffected by mitotic entry (*4*).

To elucidate how mitosis blocks RNF8 recruitment to DSB sites, we tested whether the RNF8-MDC1 interaction (*13*–*15*) is disabled in mitosis (see supplementary materials and methods). We observed that whereas RNF8 and MDC1 interact in asynchronously dividing cells after irradiation, their interaction is suppressed during M (mitotic) phase (Fig. 1A and fig. S1A; details of all synchronization and treatments are depicted in fig. S2). Because RNF8 recognizes redundant, phosphorylated epitopes on MDC1, we assessed whether mitosis inhibits the ability of RNF8 to recognize phospho-MDC1. MDC1-derived phosphopeptides that encompass its Thr^{752} (T752) phosphorylation site (pT752) are unable to retrieve RNF8 from mitotic extracts, whereas they readily retrieve RNF8 from extracts of asynchronously dividing cells (Fig. 1B and fig. S1B). This inhibition is due to cyclin-dependent kinase 1 (CDK1)–dependent phosphorylation, because pretreating mitotic extracts with PP1, a Ser/Thr phosphatase, or treating cells with the CDK1 inhibitor RO-3306 before harvesting restored the RNF8-pT752 interaction (Fig. 1B).

To test whether CDK1 could directly inhibit the RNF8-MDC1 interaction, recombinant human and mouse RNF8 proteins fused to glutathione *S*-transferase (GST) were subjected to phosphorylation by CDK1-cyclin B or CDK2-cyclin A before pull-down assays with pT752. CDK1, but not CDK2, could phosphorylate RNF8, which suppressed the ability of RNF8 to bind to pT752 (fig. S1, C to E). The reconstitution of the CDK1-dependent inhibition of the RNF8-pT752 interaction identified T198 as the main CDK1 site on RNF8 (fig. S1F). An antibody against the phosphorylated T198 residue (RNF8 pT198) confirmed a mitosis-specific phosphorylation of T198 (Fig. 1C and fig. S1G). Mutation of T198 to alanine (yielding RNF8 T198A) rendered the RNF8-pT752 interaction insensitive to CDK1 in pull-down assays (fig. S1E). In contrast, the T198E (E, Glu) mutation, which mimics T198 phosphorylation, constitutively inhibited RNF8 binding to phosphopeptides (fig. S1E).

We tested whether the RNF8-T198A mutation restored RNF8 recruitment to DSB sites in mitotic U2OS cells. Reintroduction of wild-type (WT) RNF8

[1]The Lunenfeld-Tanenbaum Research Institute, Mount Sinai Hospital, 600 University Avenue, Toronto, Ontario M5G 1X5, Canada. [2]Department of Molecular Genetics, University of Toronto, Ontario M5S 3E1, Canada.

*Corresponding author. E-mail: durocher@lunenfeld.ca